International Journal of Heat and Fluid Flow 29 (2008) 1688–1698

Contents lists available at ScienceDirect

International Journal of Heat and Fluid Flow

journal homepage: www.elsevier.com/locate/ijhff

Experimental and numerical investigations of a turbulent round jet into a cavity

Rüdiger Schwarze *, Jens Klostermann, Christoph Brücker

Institut für Mechanik und Fluiddynamik, TU Bergakademie Freiberg, Lampadiusstrasse 4, 09596 Freiberg, Germany

ARTICLE INFO

Article history:
Received 24 August 2007
Received in revised form 24 June 2008
Accepted 14 August 2008
Available online 5 October 2008

Keywords:
Jet flow
Cavity
URANS simulation
Turbulence models
Reynolds stress model
Strouhal number
Anisotropy invariant map

ABSTRACT

Turbulent flows of submerged jets into cavities are often found in technical applications. These flows tend to exhibit an oscillating behavior of large coherent structures, even in the case of steady-state boundary conditions. The paper studies basic features of a submerged jet which is injected in a cuboid volume.

The flow is investigated both experimentally and numerically. The numerical simulations are based on the unsteady Reynolds-averaged Navier–Stokes equations (URANS approach). Common two-equation and Reynolds stress turbulence models are employed in the simulations, respectively.

Mean flow fields, long-term coherent flow oscillations and flow turbulence are examined. It is found, that the results of the numerical simulations are in reasonable agreement with the experimental data. However, only numerical simulations with the Reynolds stress turbulence model resolve the long-term flow oscillations correctly. Anisotropy invariant mapping of the turbulence data from the simulations is employed in order to enlighten these findings.

© 2008 Elsevier Inc. All rights reserved.

1. Introduction

Turbulent flows of submerged jets in cavities are found in numerous technical applications, e.g. in continuously feeded reactors, in continuous casting tundishes for steelmaking or in sewage treatment ponds and tanks. These high Reynolds number flows often exhibit a long-term oscillating behavior of large coherent structures, even in the case of steady-state boundary conditions (Nikiforaki et al., 2003; Worth and Yang, 2006; Schwarze and Obermeier, 2007). The oscillations may lead to problems in process control. As an example, long-term flow oscillations may cause resuspension of sediment from the bottom of settling ponds in sewage plants, see the discussion in De Clercq (2003). Therefore detailed knowledge of these flows is of fundamental importance in order to improve process control and process performance.

The paper presents a basic model for these flows, which consists of a turbulent round jet which is injected into a cuboid volume. The jet axis is perpendicular to the cavity mean axis. Fig. 1 shows basic features of the cavity flow: (1) jet flow downstream of the inlet pipe, (2), (3) recirculating regions around the jet and (4) bypass flow towards the outlet. The present study is complementary to the paper of Mataoui et al. (2001), who investigated a planar jet which is injected parallel to the mean axis of a rectangular cavity.

Experimental and numerical investigations of the flow are presented. Measurements are done with pressure tubes and Laser Doppler anemometry (LDA). A complete resolution of the unsteady flow fields by means of direct numerical simulation is out of scope. Large eddy simulations of the turbulent flows would be very time- and memory-consuming, too. Therefore numerical simulations which are based on the unsteady Reynolds-averaged Navier–Stokes equations (URANS approach) (Mataoui et al., 2001; Johansson et al., 1993; Durbin, 1995; Kenjeres and Hanjalic, 1999; Iaccarino et al., 2003; Wegner et al., 2004; Lardeau and Leschziner, 2005; Schwarze, 2006) are performed. Here, only the oscillations of the large coherent structures are resolved, whereas all turbulent scales are modelled. The k–ϵ two-equation and the Reynolds stress turbulence models are employed in combination with wall functions in order to approximate the turbulence quantities in the flow.

Mean flow fields, long-term coherent flow oscillations and flow turbulence are examined. The physical mechanism of self-sustained coherent vortex generation is explained. The quality assessment of the employed turbulence models is different. Invariants of the anisotropy tensor of the turbulence in the simulations are analyzed in order to clarify these findings.

2. Experiment

2.1. Water model facility

The main component of the experimental facility is the cavity made of perspex. The dimensions of the flow geometry under investigation are displayed in Fig. 2. The center of the inlet pipe is located at $x_1 = 125$ mm, $x_2 = 125$ mm, the center of the outlet pipe is located at $x_1 = 875$ mm, $x_2 = 125$ mm. The model is fed by a water circuit, Fig. 3a. The density of the water is $\rho = 1000 kg/m^3$,

* Corresponding author. Tel.: +49 3731 392486; fax: +49 3731 393455.
E-mail address: Ruediger.Schwarze@imfd.tu-freiberg.de (R. Schwarze).

0142-727X/$ - see front matter © 2008 Elsevier Inc. All rights reserved.
doi:10.1016/j.ijheatfluidflow.2008.08.001

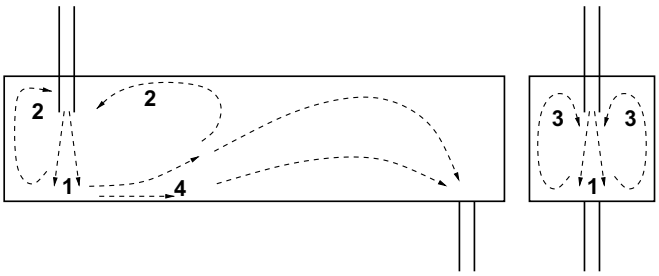

Fig. 1. Basic flow structure in the cavity.

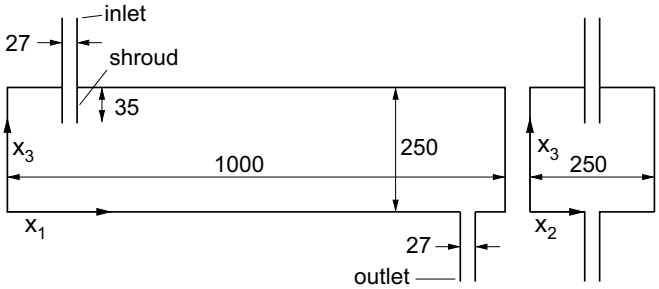

Fig. 2. Dimensions of the cavity given in mm.

its kinematic viscosity is $\nu = 10^{-6}$ m^2/s. The water enters and leaves the cavity laterally through pipes. The pipe diameter is $d = 27$ mm. The flow rate in the model is tuned by a valve between $\dot{V} = 1.6$–2.2 l/s, which correspond to jet flow Reynolds numbers $Re_j = 4\dot{V}/(\pi\nu d) = 7.5 \times 10^4$–$1 \times 10^5$ and to bulk cross flow Reynolds numbers $Re_{cf} = 4\dot{V}/(\nu h) = 6400$–$8800$, where $h = 250$ mm is the height of the cavity.

Velocity data inside the cavity are obtained from a LDA (2D Dantec Dynamics) system, Fig. 3b. The LDA measurements should resolve mean and root mean square (rms) velocity values. The measurements are performed on a 10 mm × 10 mm grid in different planes in the cavity, Fig. 3c and Table 1. Plane L1 corresponds to the vertical longitudinal midplane of the cavity, plane L2 is parallel to L1 but shifted towards the side wall of the cavity. Plane C1 is the lateral cross section through the center of the inlet jet, plane C2 is the lateral cross section through the center of the cavity. Plane H is a horizontally oriented surface just below the top lid of the cavity. The LDA measurements have been performed for a flow rate $\dot{V} = 2.2$ l/s ($Re_{cf} = 8800$). Data acquisition rates are about 100 Hz. The sampling time in each point of the measurements planes is limited to 10 s due to the available storage space of the LDA system.

Pressure time series are measured with a pressure tube (orifice diameter 3 mm), which is connected to a pressure transducer (Kistler). The pressure measurements should resolve the frequencies of the coherent oscillations and turbulent fluctuations of the flow fields. The time series are recorded at different locations within the cavity, Table 2. Point PM1 is in the front corner of the cavity near to the inlet jet, PM2 is near to the center of the cavity and PM3 is located towards the outlet region of the cavity. The data acquisition rate is 20 Hz, sampling time is 500 s in each point.

3. Numerical model

3.1. Model equations

The model equations for the URANS approach are

$$\frac{\partial\langle u_i\rangle}{\partial x_i} = 0 \tag{1}$$

$$\rho\frac{\partial\langle u_i\rangle}{\partial t} + \rho\frac{\partial}{\partial x_j}(\langle u_j\rangle\langle u_i\rangle) = -\frac{\partial\langle p\rangle}{\partial x_i} + \rho\nu\frac{\partial^2\langle u_i\rangle}{\partial x_j^2} + \frac{\partial\tau_{ij}}{\partial x_j} \tag{2}$$

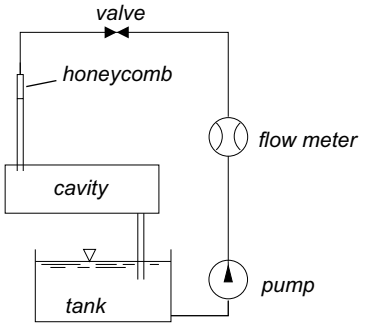

(a) water circuit

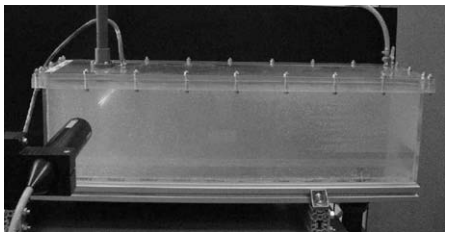

(b) LDA measurement

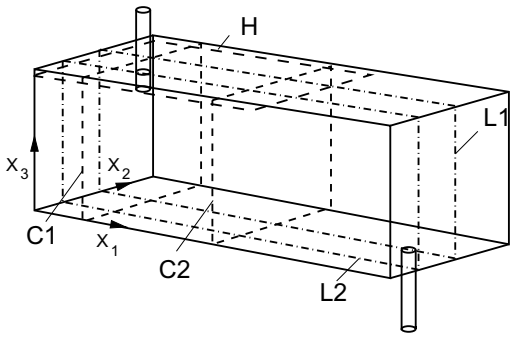

(c) measurement planes

Fig. 3. Water model facility.

Table 1
Locations of LDA measurement planes in the cavity

Name	x_1 (mm)	x_2 (mm)	x_3 (mm)
L1	0–1000	125	0–250
L2	0–1000	68	0–250
C1	125	0–250	0–250
C2	500	0–250	0–250
H	0–600	0–250	240

Table 2
Locations of pressure measurements in the cavity

Name	x_1 (mm)	x_2 (mm)	x_3 (mm)
PM1	50	50	200
PM2	500	125	200
PM3	750	125	120

Here $\langle u \rangle$ is the ensemble averaged velocity and $\langle p \rangle$ is the ensemble averaged pressure, where brackets $\langle \cdots \rangle$ indicate the resolved quantities. The ensemble averaging procedure is assumed to be implicitly applied to the fundamental flow equations (Hanjalic and Kenjeres, 2001). The unknown Reynolds stresses $\tau_{ij} = -\rho[\langle u_i u_j \rangle - \langle u_i \rangle \langle u_j \rangle]$ in (2) are provided by a turbulence model.

The standard k–ϵ model (Launder and Spalding, 1974) (KE) or alternatively the Reynolds stress model (Launder et al., 1975) (RS) are employed in the simulations. These turbulence models contain parameters, which are adjusted to reproduce turbulence in statistically steady flows whereas the oscillating flows under consideration are statistically unsteady. We assume, that the corresponding model errors are small, because the periods of the coherent oscillations are large compared with the largest time scales of the turbulent fluctuations.

In the KE model, transport equations for the turbulent kinetic energy k and the dissipation ϵ are solved. The link between the KE model and the Reynolds stresses is given by Boussinesq approach

$$\tau_{ij} = 2\rho \nu_t S_{ij} - \frac{2}{3}\rho k \delta_{ij} \tag{3}$$

$$S_{ij} = \frac{1}{2}\left(\frac{\partial \langle u_i \rangle}{\partial x_j} + \frac{\partial \langle u_j \rangle}{\partial x_i}\right) \tag{4}$$

where ν_t is the turbulent viscosity and S_{ij} is the strain-rate tensor. In the RS model, transport equations for the individual Reynolds stresses τ_{ij} and the dissipation ϵ are solved. The transport equations for the Reynolds stresses are

$$\frac{\partial \tau_{ij}}{\partial t} + \frac{\partial}{\partial x_k}(\langle u_k \rangle \tau_{ij}) = P_{ij} + D_{ij} + \phi_{ij} + \epsilon_{ij} \tag{5}$$

with the production P_{ij}, diffusion D_{ij}, pressure-strain ϕ_{ij} and dissipation term ϵ_{ij}, where D_{ij} is approximated due to the proposal of Lien and Leschziner (1994) and ϕ_{ij} is modelled due to Gibson and Launder (1978). The equations of the Reynolds stress model are given in the Appendix.

3.2. Boundary conditions and initial values

The cavity flow is dominated by the interaction of the jet flow, free shear layers and large recirculating regions, see Fig. 1. The wall shear layers are of minor importance for understanding the cavity flow, therefore non-equilibrium wall functions (Kim and and Choudhury, 1995) are employed in order to describe the near-wall regions. The wall functions are given in the Appendix, too. In case of simulations with the RS model, wall-reflection terms are employed in order to describe the redistribution of normal stresses near to the wall.

The inlet and outlet boundary conditions of the numerical simulations fit to the parameters of the experimental configuration. It has to be emphasized that the boundary conditions are steady-state conditions even in the unsteady simulations. The inlet is located 523 mm upstream in the incoming pipe. Here the inlet velocity U_{in} is fixed with respect to the resulting constant flow rate $\dot{V} = \pi d^2 U_{\text{in}}/4$. Simulations are performed for flow rates from $\dot{V} = 1.4$ l/s ($Re_{\text{cf}} = 5600$) to $\dot{V} = 2.2$ l/s ($Re_{\text{cf}} = 8800$). In all simulations, the inlet turbulence intensity is assumed to be $\text{TI}_{\text{in}} = 5\%$. Inlet values for k, ϵ and τ_{ij} are then estimated from TI and d. The outlet is located 500 mm downstream in the outgoing pipe. Here the constant outlet pressure is set to ambient pressure $P_{\text{out}} = 100$ kPa.

We assume that the intrinsic unsteady flow behavior is independent from the start-up phase of the flow. Therefore, initial values of the simulations are estimated from a numerical solution of the model equations without the transient terms (steady-state mode) in order to accelerate the simulations. In doing so, long-term numerical simulations of the start-up and development phase of the complex flow fields are avoided. However, it was not possible to get a fully converged solution of the model equations in steady-state mode.

3.3. Numerics

The model equations are solved by the finite-volume method. Spatial discretization is done with the QUICK scheme for the convective terms and with the central differencing scheme for the diffusive terms. Time-marching is performed with an implicit second-order backward differencing scheme. These numerical schemes are similarly applied to Eqs. (1) and (2) and the turbulence model's equations.

The solution domain contains 2.2×10^5 hexahedral grid cells, Fig. 4a. An O-type grid block is located around the shrouded inlet pipe and the jet in order to resolve the shear layers of the jet

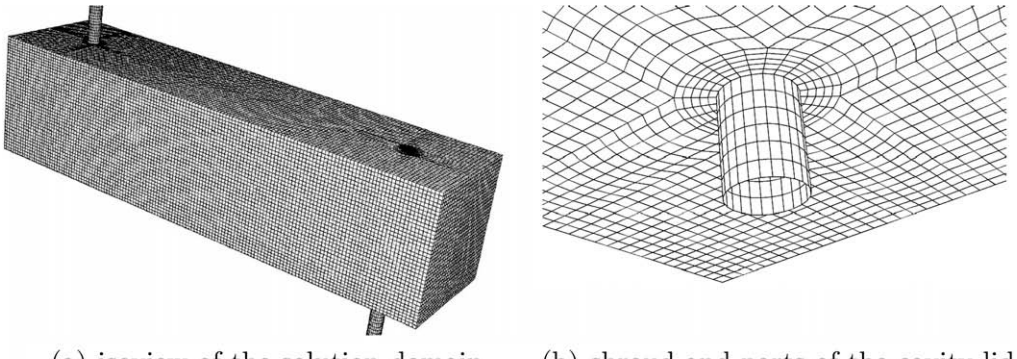

(a) isoview of the solution domain (b) shroud and parts of the cavity lid

Fig. 4. Numerical grid for the simulations.

properly, Fig. 4b. In the bulk flow region of the cavity, shapes and volumes of the grid cells are approximately constant.

Flow time intervals $\tau = 100$ s are resolved in all simulations. The SIMPLE algorithm is used to solve the flow equations iteratively. All simulations are performed with the segregated solver in Fluent 6 on 8 CPU's of a SGI Altix 3700 equipped with Intel Itanium 2 processors.

4. Results

4.1. Pressure measurements

An example of a time record of the pressure p in point PM2 for a flow rate $\dot{V} = 1.6$ l/s ($Re_{cf} = 6400$) is given in Fig. 5. The regular oscillating behavior of the pressure is evident, the oscillations can be clearly distinguished from the smaller turbulent fluctuations. All time series of pressure measurements at different locations and flow rates are analyzed by means of fast Fourier transforms (FFT).

Exemplary results are given in Figs. 6 and 7. Fig. 6 shows FFT spectra of the pressure at PM2, which are obtained for two different flow rates. Fig. 6a is the FFT spectra of the pressure time series pictured in Fig. 5, Fig. 6b gives the FFT spectra for $\dot{V} = 1.9$ l/s ($Re_{cf} = 7600$). The coherent oscillations correspond to peaks at $f_{C,exp} \sim 0.15$ Hz with smaller peaks at $f_{2C,exp} \sim 0.3$ Hz due to frequency doubling in both spectra. Scaling behavior in different frequency ranges of the FFT spectra is indicated ($f^{-5/3}$ and f^{-7}) only for orientation.

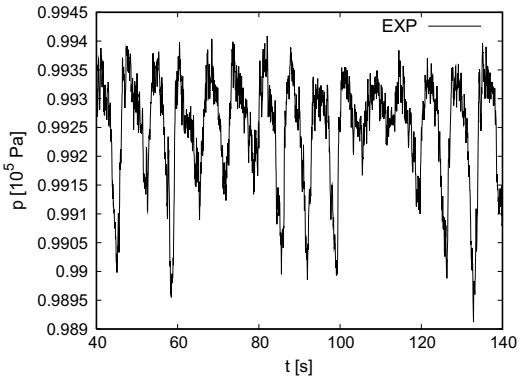

Fig. 5. Example for time series of p recorded in PM2.

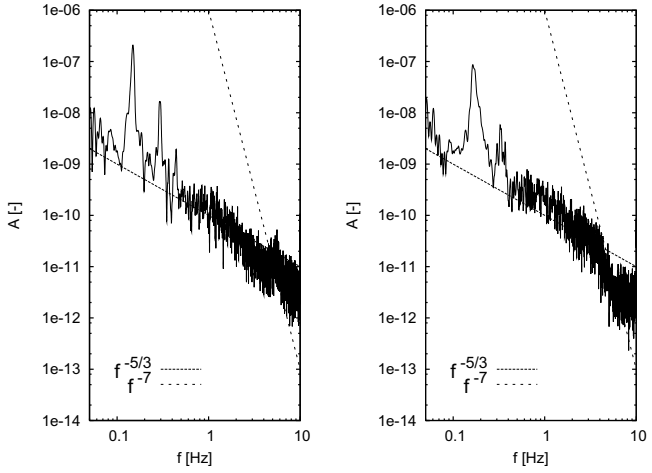

Fig. 6. FFT pressure spectra in location PM2, flow rate $\dot{V} = 1.6$ l/s (left) and $\dot{V} = 1.88$ l/s (right).

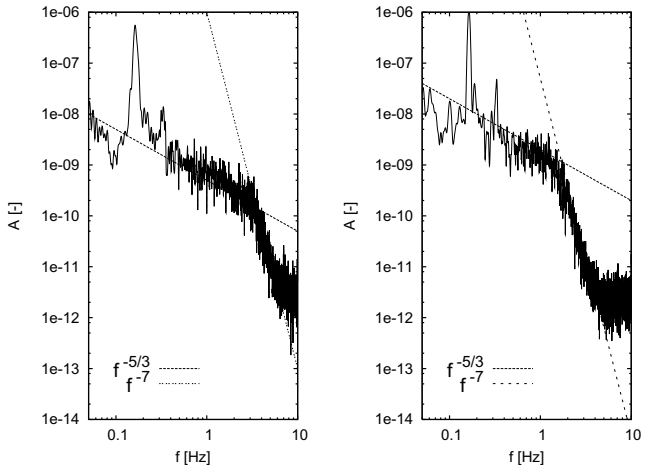

Fig. 7. FFT pressure spectra for flow rate $\dot{V} = 2.1$ l/s in location PM1 (left) and PM3 (right).

Fig. 7 gives the spectra, which are obtained for a constant flow rate $\dot{V} = 2.1$ l/s ($Re_{cf} = 8400$) in PM1 and PM3. Again, clear peaks are found at $f_{C,exp} \sim 0.15$ Hz in both spectra.

4.2. Mean flow field

Mean values of the velocity in the experiments (exp) and in the simulations (num) are evaluated as follows:

$$U_{i,exp} = \frac{1}{\Delta t}\int_{t_0}^{t_0+\Delta t} u_i \mathrm{d}t \tag{6}$$

$$U_{i,num} = \frac{1}{\Delta t}\int_{t_0}^{t_0+\Delta t} \langle u_i \rangle \mathrm{d}t \tag{7}$$

Root mean square (rms) values of the velocity are calculated as follows:

$$u_{i,rms,exp} = \frac{1}{\Delta t}\int_{t_0}^{t_0+\Delta t} \sqrt{(u_i - U_i)^2}\mathrm{d}t \tag{8}$$

$$u_{i,rms,num} = \frac{1}{\Delta t}\int_{t_0}^{t_0+\Delta t} \left[\sqrt{(\langle u_i \rangle - U_i)^2} + \sqrt{\frac{\tau_{ii}}{\rho}}\right]\mathrm{d}t \tag{9}$$

where no summation is performed for τ_{ii}. As explained in Section 2, the averaging period in the LDA data is $\Delta t = 10s$. For convenience the numerical data is averaged over the same period. In case of URANS simulations with the KE model, the instantaneous Reynolds stresses τ_{ii} are deduced from Eq. (3). In case of URANS simulations with the RS model, the instantaneous Reynolds stresses τ_{ii} are obtained from the solution of Eq. (5).

Figs. 8–10 display exemplary numerical results of the mean velocity amplitude $U = \sqrt{U_i U_i}$ for the flow rate $\dot{V} = 2.2$ l/s ($Re_{cf} = 8800$). In the figures, contour plots are given for planes L1 (Fig. 8), L2 (Fig. 9) and C1 (Fig. 10). High velocities are light colored and low velocities are dark colored, respectively. Additionally, streamlines are indicated in order to reveal the basic flow structures. In accordance with Fig. 1, the inlet jet (1) is found in plane L1 and C1 (Figs. 8 and 10). Recirculating regions (2,3) are evident in all planes. Finally, the bypass flow (4) is identified in planes L1 and L2 (Figs. 8 and 9).

4.3. Mean value profiles of the velocity field

Figs. 11–13 show profiles of U_i and $u_{i,rms}$ along longitudinal and lateral lines in the cavity. In the figures, data from the LDA measurements (EXP), URANS simulations with the k–ϵ (KE) and the Reynolds stress (RS) model are compared.

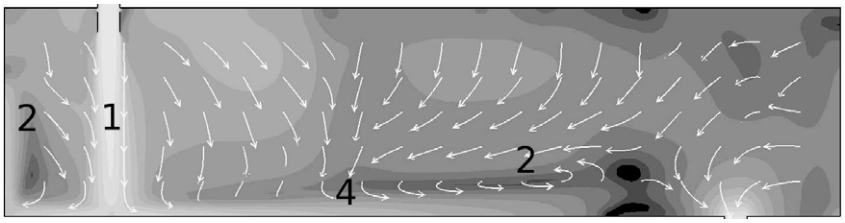

Fig. 8. Streamlines and contour plot of the mean velocity field in plane L1.

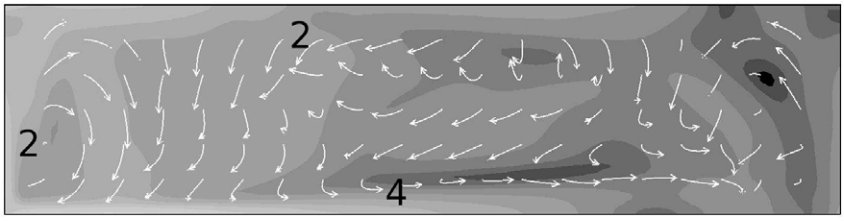

Fig. 9. Streamlines and contour plot of the mean velocity field in plane L2.

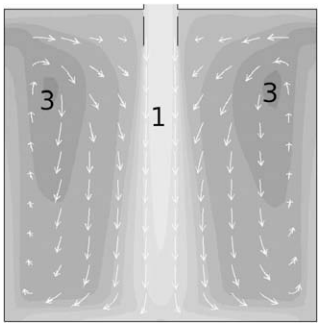

Fig. 10. Streamlines and contour plot of the mean velocity field in plane C1.

Fig. 11 displays the longitudinal velocity U_1 and $u_{1,\mathrm{rms}}$ along a longitudinal horizontal line in plane L1. The core of the inlet jet can be identified at $x_1 = 125$ mm. The measurements show a crossflow through the jet, i.e. $U_1 > 0$ for $0 < x_1 < 150$ mm. Then a wake with low values of U_1 is found for $150\ \mathrm{mm} < x_1 < 350$ mm. Finally, a backflow region with $U_1 < 0$ is evident for $x_1 > 350$ mm. In the simulation with the RS model, the directions and magnitudes of U_1 in the crossflow, wake and backflow region are well resolved. In the simulation with the KE, only the overall flow structure is acceptable resolved with a slight overprediction of the wake length, whereas the amplitude of U_1 in the wake region is strongly overestimated. For the rms profiles $u_{1,\mathrm{rms}}$, it is found that all simulations give a reasonable prediction of the jet shear layer profiles at $x_1 = 120$ mm and $x_1 = 150$ mm. In the wake, KE underpredicts and RS overestimates the rms values. In the backflow, all simulations are in good agreement with the experiment.

Fig. 12 displays U_1 and $u_{1,\mathrm{rms}}$ of the longitudinal velocity along a longitudinal horizontal line in plane L2. The noticeable feature in the measurements of U_1 is a backflow region with $U_1 < 0$ for $200\ \mathrm{mm} < x_1 < 500$ mm. The simulation with the RS model resolves the flow reversal at $x_1 \simeq 200$ mm but overestimates the length of the backflow region, whereas the simulation with the KE gives a wrong slope of the profile for $x_1 > 200$ mm. For the rms profiles $u_{1,\mathrm{rms}}$, the RS model is in good agreement with the measurements, but the KE model underpredicts the rms values.

Fig. 13 displays the vertical velocity U_3 and $u_{3,\mathrm{rms}}$ along a lateral horizontal line in plane C1. The shape of the jet can be clearly identified in U_3. In the jet core, both URANS simulations RS and KE overestimate U_3 slightly. In the shear layers and the outer parts of the profiles, the experimental and numerical results are in good agreement. Regarding the profiles of $u_{3,\mathrm{rms}}$, the agreement between experimental and numerical data is good in the outer parts. In the jet shear layers, RS overpredicts the peak values, whereas KE underestimates the rms values significantly.

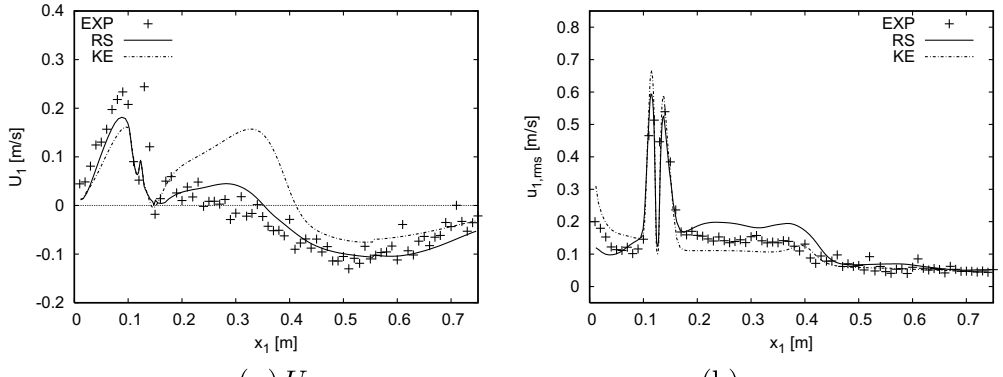

(a) U_1 (b) $u_{1,rms}$

Fig. 11. Velocity profile at $x_2 = 125$ mm and $x_3 = 100$ mm.

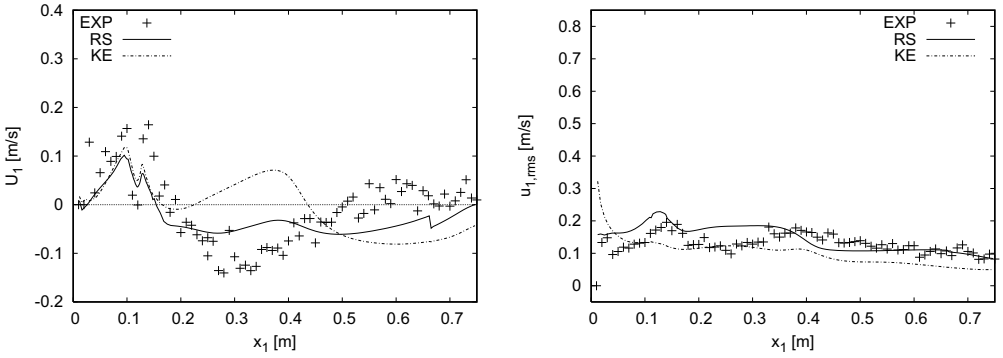

(a) U_1 (b) $u_{1,rms}$

Fig. 12. Velocity profile at x_2 = 68 mm and x_3 = 50 mm.

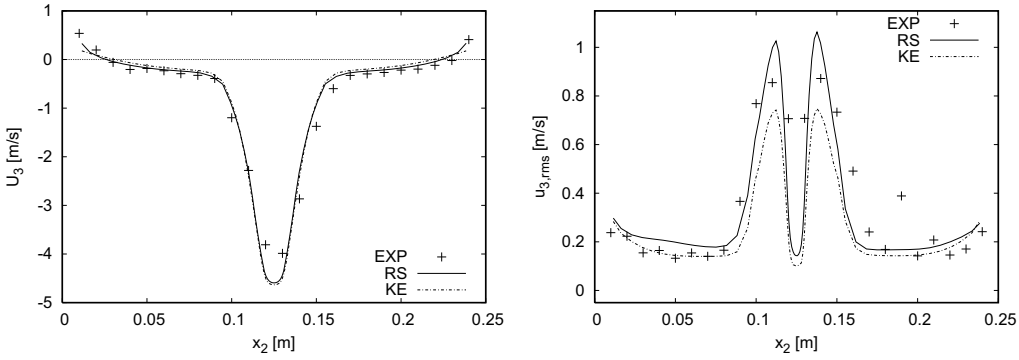

(a) U_3 (b) $u_{3,rms}$

Fig. 13. Velocity profiles at x_1 = 125 mm and x_3 = 100 mm.

The contributions of the resolved coherent oscillations (res) and modelled turbulent fluctuations (mod) to the total rms velocity are exemplary pictured in Fig. 14. Here, $u_{i,\mathrm{rms,res}}$ and $u_{i,\mathrm{rms,mod}}$ are defined as follows:

$$u_{i,\mathrm{rms,res}} = \frac{1}{\Delta t}\int_{t_0}^{t_0+\Delta t}\sqrt{(\langle u_i\rangle - U_i)^2}\,\mathrm{d}t \tag{10}$$

$$u_{i,\mathrm{rms,mod}} = \frac{1}{\Delta t}\int_{t_0}^{t_0+\Delta t}\sqrt{\frac{\tau_{ii}}{\rho}}\,\mathrm{d}t \tag{11}$$

Fig. 14 shows that the portions of the resolved coherent oscillations and the modelled turbulent fluctuations of the total rms velocity depend on the location in the flow. In the longitudinal profile at x_2 = 125 mm and x_3 = 100 mm the simulation with the KE model seems to underpredict the contributions of the resolved velocity oscillations $u_{1,\mathrm{rms,res}}$ (KE, res), they are much smaller than $u_{1,\mathrm{rms,mod}}$ (KE, mod) in Fig. 14a. The underprediction of the total rms velocity may be caused by this deficiency. We assume, that the very dissipative nature of the KE model tends to damp the coherent oscillations down.

Contrary, $u_{1,\mathrm{rms,res}}$ (RS, res) is in the same order of magnitude as $u_{1,\mathrm{rms,mod}}$ (RS, mod) in the simulation with the RS model, Fig. 14b. Here the total rms velocity is overrated, especially in the backflow region. It is not clear if this error is caused by an overprediction of the resolved velocity oscillations or by an overestimation of the turbulence.

Comparing Figs. 14a and b, it is found that the variations between the profiles of $u_{1,\mathrm{rms,mod}}$ from the KE and the RS model are much smaller than the differences between the profiles of $u_{1,\mathrm{rms,res}}$. Similar findings result from the comparison of the profiles of $u_{1,\mathrm{rms,res}}$ and $u_{1,\mathrm{rms,mod}}$ in the jet flow region, Figs. 14c and d.

4.4. Oscillating flow field

The complex structure of the unsteady cavity flow is visualized in Figs. 15–18. Here streamlines in the results of the URANS simulations for the flow rate $\dot{V} = 2.2$ l/s (Re_{cf} = 8800) are displayed.

With respect to the corresponding plots of the mean velocity fields in Figs. 8–10, it is found that the recirculating regions in planes L1 and L2 ((2) in Figs. 8 and 9) and planes C1 and C2 ((3) in Fig. 9) change their position and size in an oscillating manner. Contrary, the positions of the jet ((1) in Figs. 8 and 10) and the bypass flow ((4) in Figs. 8 and 9) remain nearly fixed.

In Fig. 18, streamlines in combination with the vorticity component ω_3

$$\omega_3 = \frac{\partial\langle u_1\rangle}{\partial x_2} - \frac{\partial\langle u_2\rangle}{\partial x_1} \tag{12}$$

and the strain rate in the horizontal plane H are displayed. The darker the color, the higher is ω_3 in Fig. 18a, whereas the lighter the color, the higher is the strain rate in Fig. 18b. A large coherent vortex is found in both subfigures. The coherent vortex in a turbulent flow is defined due to Lesieur (2008, pp. 7–8): it is a region of space,

- where vorticity concentrates enough so that fluid trajectories can wind around,
- which keeps (following the flow motion) a characteristic shape during a life time longer enough in front of their turnover time,
- which is unpredictable.

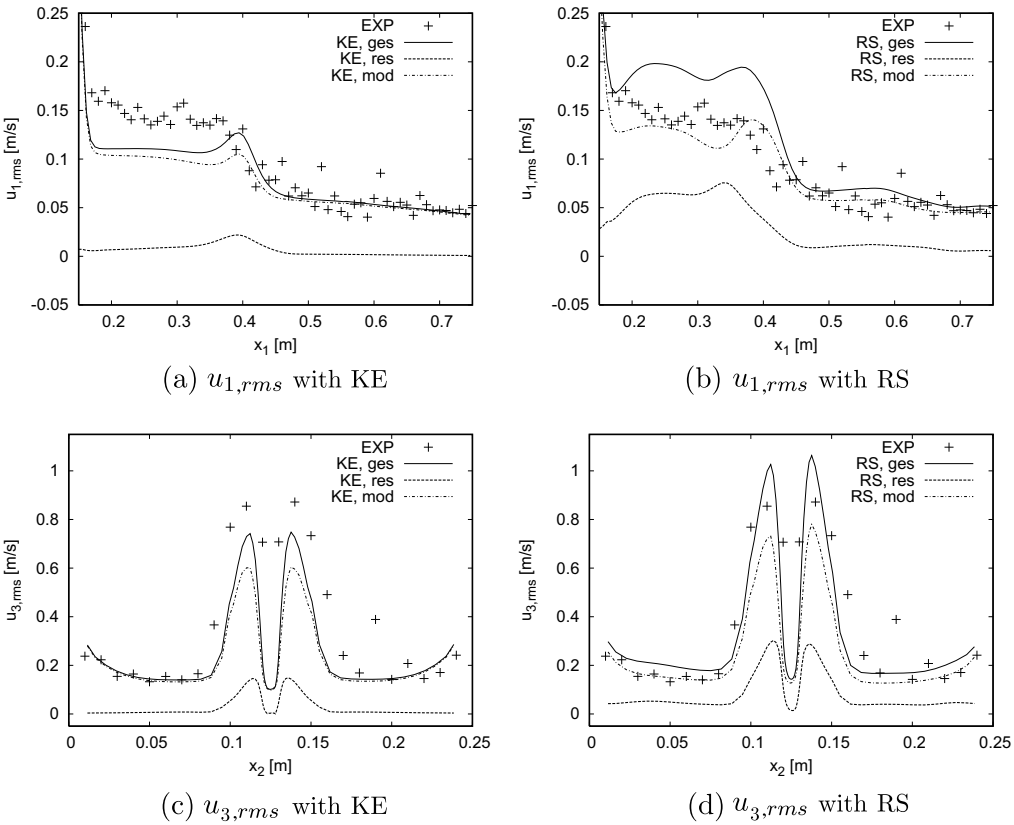

Fig. 14. Resolved and modelled contributions to the rms velocity profiles at $x_2 = 125$ mm and $x_3 = 100$ mm (subfigures (a), (b)) and at $x_1 = 125$ mm and $x_3 = 100$ mm (subfigures (c), (d)).

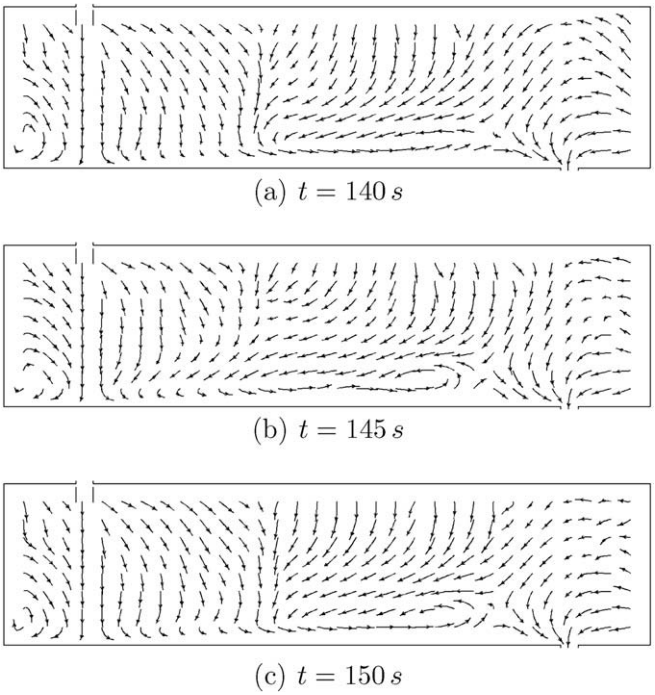

Fig. 15. Streamlines in the instantaneous flow fields in plane L1.

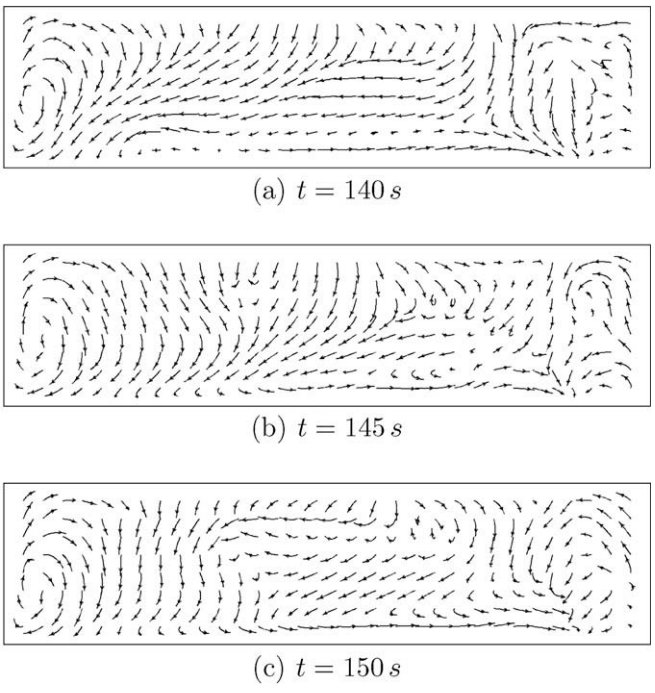

Fig. 16. Streamlines in the instantaneous flow fields in plane L2.

The coherent vortex in the cavity flow fulfills these criteria. It shows a strong oscillating behavior, which is resolved in the URANS simulations.

The shroud with its wake flow is located on the left-hand side, see Fig. 18. It is found, that ω_3 is concentrated in the recirculating regions of the shroud wake flow, in large coherent vortex structures, where the streamlines wind around and in elongated vortex layers where the streamlines are only slightly curved, Fig. 18a. Fig. 18b shows, that the vortex layers are correlated with regions of high strain rate, whereas the strain rate in the vortex is only

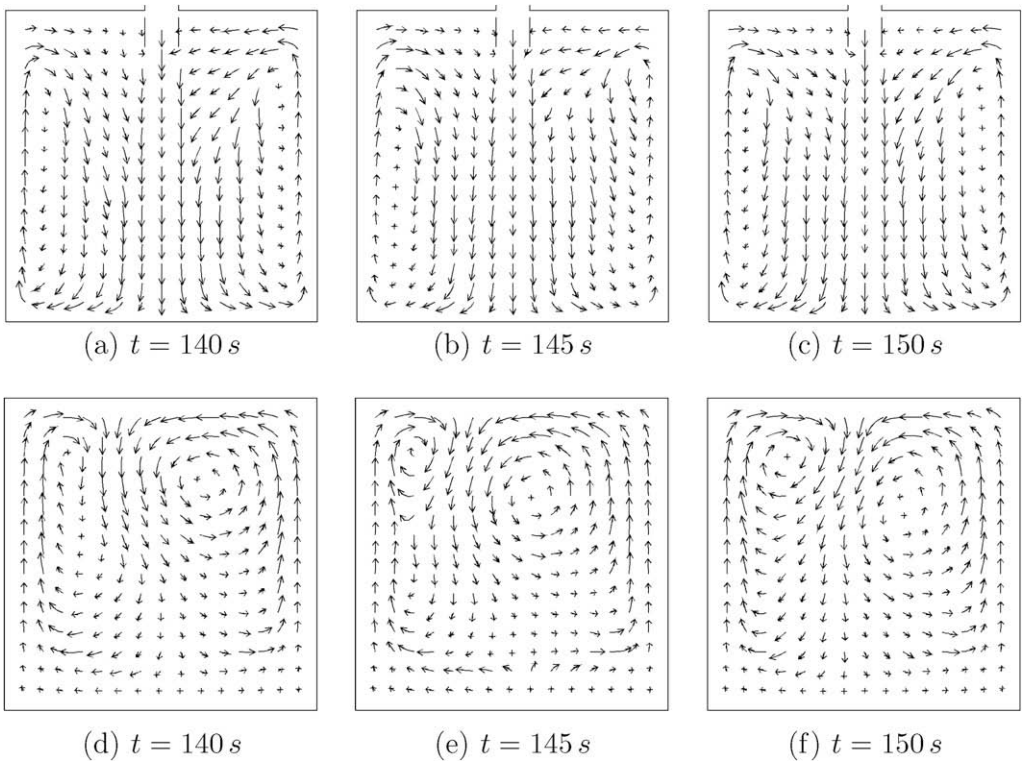

Fig. 17. Streamlines in the instantaneous flow fields, first row: plane C1, second row: plane C2.

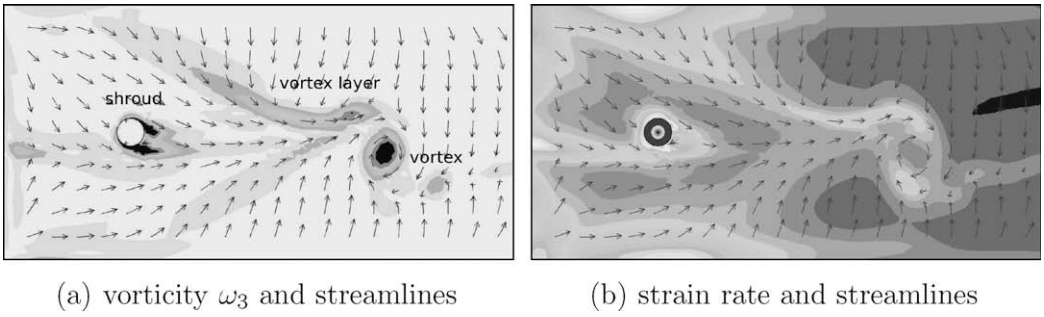

Fig. 18. Instantaneous flow field with coherent structures in plane H at $t = 140$ s.

moderate. Strain rate and vorticity are produced by the merging longitudinal (from left to the right in Fig. 18b) and lateral (from the upper and the lower wall to the centerline in Fig. 18b) flows.

The physical mechanism of the quasi-periodic vortex generation is explained in more detail in Fig. 19. In the transient flow field, the typical process of vortex formation and decay can be identified: A vortex layer is rolling-up and forms a vortex core. The vorticity of the vortex layer is fed into the vortex core, where a high value of ω_3 is induced. The lateral flow finally cuts the vortex core from the vortex layer. The detached vortex decays rapidly due to the action of the turbulent Reynolds stresses. In Fig. 19, the formation and decay of vortex structures (V1, V2, ...) due to the rolling-up of vortex layers (VL2, VL3, ...) can be clearly identified. As an example, vortex layer VL2 ($t = 140$ s) is rolling-up and forms vortex V2. V2 has been cut form the vortex layer due to action from the upper lateral flow at $t = 141$ s and decays ($t = 141$ s and $t = 142$ s). The upper lateral flow and the swirling flow around V2 drive the longitudinal flow towards the lower wall and induce a new vortex layer VL3. The next vortex V3 is formed by the rolling-up of VL3 and so on.

These complex interactions of vortex layers and large recirculation are assumed to be responsible for the intrinsic unsteadiness of the cavity flow.

For quantitative analysis, time series of the lateral velocity $\langle u_2 \rangle$ are recorded at point UR ($x_1 = 250$ mm, $x_2 = 125$ mm, $x_3 = 200$ mm). As an example, Fig. 20 gives the time series $\langle u_2 \rangle$ which is obtained in a simulation with the RS model for the flow rate $\dot{V} = 1.60$ l/s ($Re_{cf} = 6400$). Fig. 21 gives the corresponding FFT spectrum of this time series with linear–linear and log–log axis scaling, respectively. The linear–linear plot reveals a clear frequency peak $f_{C,sim} \simeq 0.15$ Hz which corresponds to the coherent oscillation of the cavity flow. The log–log plot enlightens the action of the turbulence model, i.e. only low frequencies are resolved in the simulations. Contrary the turbulent frequencies are removed from the spectrum because turbulent fluctuations are strongly damped.

The resulting peak frequencies of the pressure measurements and URANS simulations with the KE and the RS model are compared in Fig. 22. Here, the Strouhal number St_C of the coherent oscillation is defined as

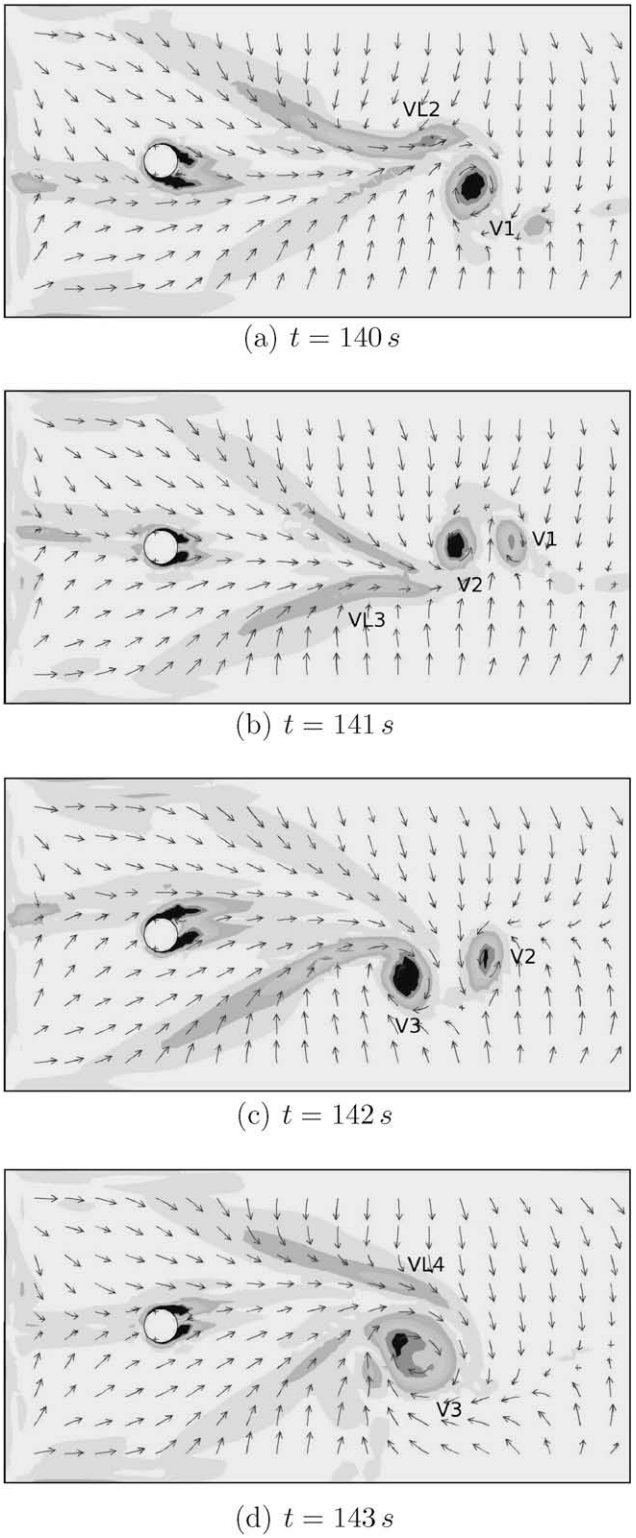

Fig. 19. Development and decay of coherent vortex structures in the flow, vorticity component ω_3 and streamlines are plotted in plane H.

$$St_C = \frac{f_C d}{u_{cf}} = \frac{f_C dwh}{\dot{V}} \tag{13}$$

where $w = 250$ mm is the width of the cavity. The measurements show a nearly constant Strouhal number $St_{C,exp} \simeq 0.14$.

Numerical simulations with the RS model give also a nearly constant Strouhal number $St_{C,RS} \simeq 0.17$, which is noticable higher

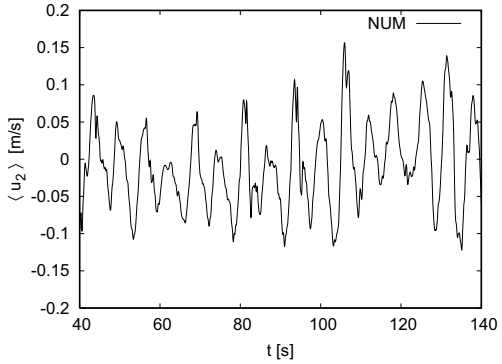

Fig. 20. Time series of $\langle u_2 \rangle$ in point UR ($x_1 = 250$ mm, $x_2 = 125$ mm, $x_3 = 200$ mm).

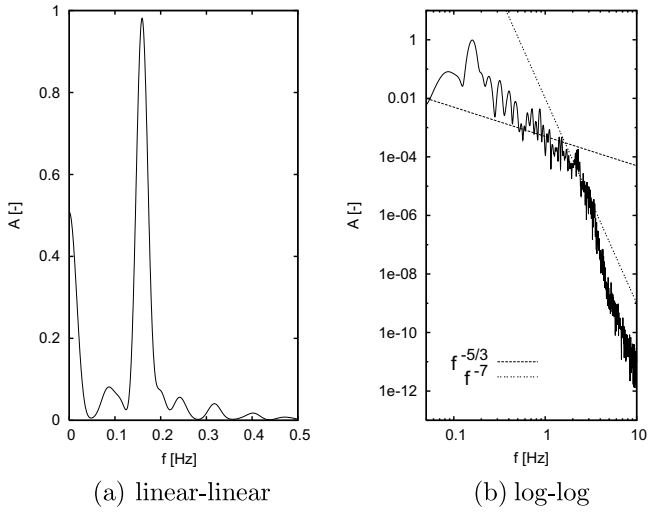

Fig. 21. FFT spectra from URANS data of $\langle u_2 \rangle$ in point UR.

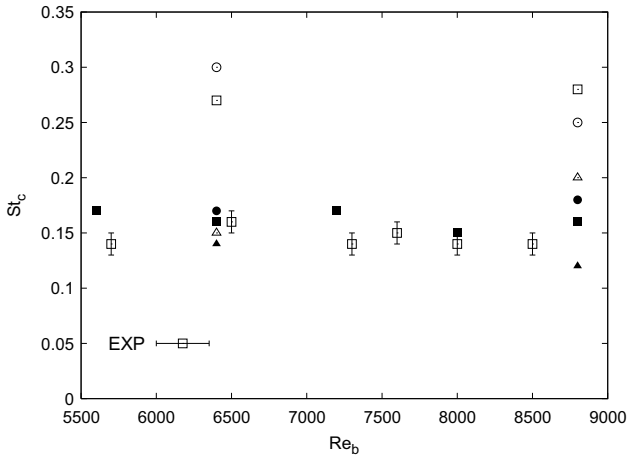

Fig. 22. Plot of Strouhal number versus Reynolds number for experiments and numerical simulations. Filled symbols are from the RS model, open symbols are from the KE model, time step widths are $\Delta t_1^{num} = 0.1$ s (▲,△), $\Delta t_2^{num} = 0.05$ s (■,□) and $\Delta t_3^{num} = 0.025$ s (●,○).

than in the measurements. The simulations for the flow rates $\dot{V} = 1.6\,l/s$ ($Re_{cf} = 6400$) and $\dot{V} = 2.2$ l/s ($Re_{cf} = 8800$) are performed with three time step widths $\Delta t_1^{num} = 0.1$ s, $\Delta t_2^{num} = 0.05$ s and $\Delta t_3^{num} = 0.025$ s in order to judge the convergence of the resolved flow oscillations. Although complete convergence is not

found, the differences in $St_{C,RS}$ decrease successively from Δt_1^{num} to Δt_3^{num}. Contrary, numerical simulations with the KE model give a much higher Strouhal number $St_{C,KE} \simeq 0.28$ for the flow oscillation.

The invariants II_a and III_a of the anisotropy tensor a_{ij} (Lumley and Newman, 1977)

$$a_{ij} = \frac{\tau_{ij}}{\tau_{kk}} - \frac{1}{3}\delta_{ij} \tag{14}$$

$$II_a = a_{ij}a_{ji} \tag{15}$$

$$III_a = a_{ij}a_{jk}a_{ki} \tag{16}$$

are investigated in order to explain these findings. In case of URANS simulations with the KE model, the Reynolds stresses τ_{ij} are deduced from Eq. (3), whereas in case of URANS simulations with the RS model, τ_{ij} are obtained from the solution of Eq. (5).

In incompressible flows, the first invariant $I_a = a_{kk}$ is always zero. The anisotropy invariant map is found in a III_a–II_a plot (Choi and Lumley, 2001; Jovanovic, 2004), i.e. the region of allowed states of anisotropy is limited by the curves,

$$II_a = \frac{2}{9} + 2III_a \tag{17}$$

$$II_a = -\frac{3}{2}\left(\frac{4}{3}|III_a|\right)^{2/3} \tag{18}$$

The instantaneous anisotropy tensors in the simulations with the KE and the RS model are analysed. Exemplary invariant maps which are obtained from the inspection of the turbulence data in plane L1 are plotted in Fig. 23. Clearly, instantaneous pairs (III_a, II_a) of the turbulence predicted by the RS model fall well into the allowed region. Contrary, the instantaneous turbulence predicted by the KE model gives pairs (III_a, II_a) which scatter also outside the allowed region of the invariant map. These findings are confirmed by the analysis of the numerical results in other moments.

4.5. Discussion

The comparison of numerical results with experimental data demonstrates, that simulations with the RS model give considerably better results for mean values and coherent oscillation frequencies than simulations with the KE model. Inspections of the anisotropy invariant maps reveal, that only the RS model gives a realizable turbulence estimation. This is not surprising because in contradiction to the KE model, the equations of the RS model can be reformulated into a transport equation for the turbulence anisotropy (Jovanovic, 2004). Therefore, only simulations with the RS model are able to capture the dynamics of the turbulence anisotropy.

As it has been shown before, the generation of coherent structures in the flow is strongly linked to transient behavior of complex three-dimensional vortex layers, where turbulence is anisotrop. Therefore, the correct description of the anisotropy tensor is an important ingredient for an reliable URANS simulation of the unsteady cavity flow.

5. Conclusions

The flow of a turbulent round jet into a cavity is investigated both experimentally and numerically. The numerical simulations are based on the unsteady Reynolds-averaged Navier–Stokes equations (URANS approach). The standard k–ϵ and Reynolds stress turbulence models are employed in the simulations, respectively.

Mean flow fields, long-term coherent flow oscillations and flow turbulence are examined. It is found, that the flow field is highly three-dimensional due to complex links between longitudinal and lateral oriented recirculating regions and the jet flow. The recirculating regions are separated by free shear and vortex layers. The generation of coherent vortex structures in the unsteady flow is based on the quasi-periodic rolling-up of these vortex layers.

Simulations with the Reynolds stress turbulence model give considerably better results for mean values and coherent oscillation frequencies than simulations with the k–ϵ model. Inspections of the anisotropy invariant maps reveal, that only the RS model gives a realizable estimation of the turbulence, which is considerably anisotrop due to the vortex layers in the flow. A proper approximation of the anisotrop turbulence seems to be of fundamental importance for a correct simulation of the oscillating behavior of the cavity flow.

However, some noticeable differences between measurements and URANS simulations with the Reynolds stress turbulence model are still present. Especially, the root mean square values of the velocity are overestimated in some regions of the oscillating flow. Therefore, refined investigations are necessary in the future in order to clarify the reasons for these shortcomings and to improve the numerical model further.

For example, the employed turbulence models are calibrated at flows with turbulence in steady-state. It should be verified in future studies, if the corresponding model parameters need to be tuned for turbulent flows which exhibit coherent oscillations. Here, a comparison of URANS results with LES data is desirable. This comparison should also indicate, if a hybrid URANS-LES simulation will give an efficient and more accurate description of the flow. Alternatively, the turbulence model can be sensitized to the unsteady mean flow parameters in order to avoid unphysical turbulence production, e.g. in the recirculating regions.

The present paper is focused on a comparison of simulations with the standard k–ϵ and the Reynolds stress turbulence model. It would be useful to test other turbulence models in future studies, for example the realizable k–ϵ model. A two-equation model

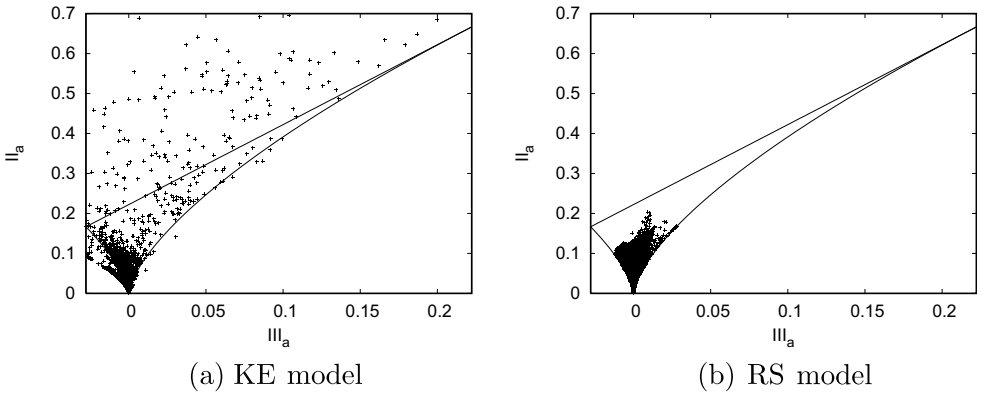

Fig. 23. Invariant map for simulations with the KE and the RS model.

can help to reduce the computational efforts especially in a hybrid URANS-LES simulation.

Appendix A. Reynolds stress model

The equations of the Reynolds stress model are

$$\frac{\partial \tau_{ij}}{\partial t} + \underbrace{\frac{\partial}{\partial x_k}\left(\langle u_k\rangle \tau_{ij}\right)}_{C_{ij}} = \underbrace{-\tau_{ik}\frac{\partial \langle u_j\rangle}{\partial x_k} - \tau_{jk}\frac{\partial \langle u_i\rangle}{\partial x_k}}_{P_{ij}} + \underbrace{\frac{\partial}{\partial x_k}\left[\frac{\nu_t}{\sigma_k}\frac{\partial \tau_{ij}}{\partial x_k}\right] + \nu\frac{\partial^2 \tau_{ij}}{\partial x_k^2}}_{D_{ij}} - \underbrace{c_1\frac{\epsilon}{k}\left[\frac{2}{3}\rho k\delta_{ij} - \tau_{ij}\right] + c_2\left[\frac{2}{3}(P-C)\delta_{ij} - (P_{ij}-C_{ij})\right]}_{\phi_{ij}} + \underbrace{\frac{2}{3}\rho\epsilon\delta_{ij}}_{\epsilon_{ij}} \tag{A.1}$$

$$\frac{\partial \epsilon}{\partial t} + \langle u_j\rangle\frac{\partial \epsilon}{\partial x_j} = \frac{\partial}{\partial x_j}\left[\left(\nu + \frac{\nu_t}{\sigma_\epsilon}\right)\frac{\partial \epsilon}{\partial x_j}\right] + c_{\epsilon 1}P\frac{\epsilon}{k} - c_{\epsilon 2}\frac{\epsilon^2}{k} \tag{A.2}$$

$$\nu_t = c_\mu\frac{k^2}{\epsilon} \tag{A.3}$$

$$k = -\frac{\tau_{jj}}{2\rho} \tag{A.4}$$

$$P = \frac{P_{jj}}{2} \tag{A.5}$$

$$C = \frac{C_{jj}}{2} \tag{A.6}$$

The coefficients in the Reynolds stress model are fixed to $\sigma_k = 0.82$, $c_1 = 1.8$, $c_2 = 0.6$, $c_\mu = 0.09$, $\sigma_\epsilon = 1.0$, $c_{\epsilon 1} = 1.44$, $c_{\epsilon 2} = 1.92$.

Appendix B. Non-equilibrium wall function

In the non-equilibrium wall function approach, the log-law of the wall is sensitized to pressure gradient effects. The resulting wall functions are

$$\langle u\rangle^+ = \frac{1}{\kappa}\ln(Ey^+) + \frac{1}{2c_\mu^{1/4}k^{1/2}}\frac{\mathrm{d}p}{\mathrm{d}x}\left[\frac{y_v}{\kappa\rho\sqrt{k}}\ln\left(\frac{y}{y_v}\right) + \frac{y-y_v}{\kappa\rho\sqrt{k}} + \frac{y_v^2}{\eta}\right] \tag{B.1}$$

$$\epsilon = \frac{c_\mu^{3/4}k^{3/2}}{\kappa y} \tag{B.2}$$

Here, y^+ is the nondimensional wall normal distance, $\langle u\rangle^+$ is the nondimensional velocity and $\mathrm{d}p/\mathrm{d}x$ the pressure gradient tangential to the wall in the wall-nearest cell, respectively.

References

Choi, K.-S., Lumley, J.L., 2001. The return to isotropy of homogeneous turbulence. J. Fluid Mech. 436, 59–84.

De Clercq, B., 2003. Computational fluid dynamics of settling tanks: development of experiments and rheological, settling, and scraper submodels. PHD Thesis, Gent University, Belgium, pp. 172–173.

Durbin, P.A., 1995. Separated flow computations with k–e–v^2 model. AIAA J. 33 (4), 659–664.

Gibson, M.M., Launder, B.E., 1978. Ground effects on pressure fluctuations in the atmospheric boundary layer. J. Fluid Mech. 86 (3), 491–511.

Hanjalic, K., Kenjeres, S., 2001. 'T-RANS' simulation of deterministic eddy structure in flows driven by thermal buoyancy and Lorentz force. Flow Turbul. Combust. 66 (4), 427–451.

Iaccarino, G., Ooi, A., Durbin, P.A., Behnia, M., 2003. Reynolds averaged simulation of unsteady separated flow. Int. J. Heat Fluid Flow 24 (2), 147–156.

Johansson, S.H., Davidson, L., Olsson, E., 1993. Numerical simulation of vortex shedding past triangular cylinders at high Reynolds number using a k–e turbulence model. Int. J. Num. Methods Fluids 16 (10), 859–878.

Jovanovic, J., 2004. The Statistical Dynamics of Turbulence. Springer-Verlag, Berlin.

Kenjeres, S., Hanjalic, K., 1999. Transient analysis of Rayleigh–Benard convection with a RANS model. Int. J. Heat Fluid Flow 20 (3), 329–340.

Kim, S.-E., Choudhury, D., 1995. A near-wall treatment using wall functions sensitized to pressure gradient. In: ASME FED – Separated and Complex Flows, vol. 217, pp. 273–280.

Lardeau, S., Leschziner, M.A., 2005. Unsteady RANS modelling of wake-blade interaction: computational requirements and limitations. Comput. Fluids 34 (1), 3–21.

Launder, B.E., Spalding, D.B., 1974. The numerical computation of turbulent flows. Comput. Methods. Appl. Mech. Eng. 3 (2), 269–289.

Launder, B.E., Reece, G.J., Rodi, W., 1975. Progress in the development of a Reynolds-stress turbulence closure. J. Fluid Mech. 68 (3), 537–566.

Lesieur, M., 2008. Turbulence of Fluids. Springer, Dordrecht.

Lien, F.S., Leschziner, M.A., 1994. Assessment of turbulence-transport models including non-linear RNG eddy-viscosity formulation and second-moment closure for flow over a backward-facing step. Comput. Fluids 23 (8), 983–1004.

Lumley, L.J., Newman, G.R., 1977. The return to isotropy of homogeneous turbulence. J. Fluid Mech. 82 (1), 161–178.

Mataoui, A., Schiestel, R., Salem, A., 2001. Flow regimes of a turbulent plane jet into a rectangular cavity: experimental approach and numerical modelling. Flow Turbul. Combust. 67 (4), 267–304.

Nikiforaki, L., Montante, G., Lee, K.C., Yianneskis, M., 2003. On the origin, frequency and magnitude of macro-instabilities of the flows in stirred vessels. Chem. Eng. Sci. 58 (13), 2937–2949.

Schwarze, R., 2006. Unsteady RANS simulation of oscillating mould flows. Int. J. Num. Methods Fluids 52 (8), 883–902.

Schwarze, R., Obermeier, F., 2007. Modelling of unsteady electromagnetically driven recirculating melt flows. Model. Simul. Mater. Sci. Eng. 12 (5), 985–993.

Wegner, B., Maltsev, A., Schneider, C., Sadiki, A., Dreizler, A., Janicka, J., 2004. Assessment of unsteady RANS in predicting swirl flow instability based on LES and experiments. Int. J. Heat Fluid Flow 25 (3), 528–536.

Worth, N.A., Yang, Z., 2006. Simulation of an impinging jet in a crossflow using a Reynolds stress transport model. Int. J. Num. Methods Fluids 52 (2), 199–211.